Human Molecular Genetics, 2012, Vol. 21, No. 17 **3858–3870**
doi:10.1093/hmg/dds214
Advance Access published on June 7, 2012

Respiratory dysfunction by AFG3L2 deficiency causes decreased mitochondrial calcium uptake via organellar network fragmentation

Francesca Maltecca[1], Diego De Stefani[2], Laura Cassina[1,4], Francesco Consolato[1,5], Michal Wasilewski[3], Luca Scorrano[3], Rosario Rizzuto[2] and Giorgio Casari[1,*]

[1]San Raffaele Scientific Institute, Vita-Salute San Raffaele University and Center for Translational Genomics and Bioinformatics, Milan-I, Italy, [2]Department of Biomedical Sciences, University of Padova, Padova-I, Italy, [3]Department of Cell Physiology and Metabolism, University of Geneva Medical School, Genève-CH, Switzerland and Dulbecco-Telethon Institute, Padova-I, Italy, [4]Department of Genetics, Biology and Biochemistry, University of Turin, Turin-I, Italy, [5]PhD school of Neurobiology, University of Insubria, Varese-I, Italy

Received April 27, 2012; Revised and Accepted May 29, 2012

The mitochondrial protein AFG3L2 forms homo-oligomeric and hetero-oligomeric complexes with paraplegin in the inner mitochondrial membrane, named *m*-AAA proteases. These complexes are in charge of quality control of misfolded proteins and participate in the regulation of OPA1 proteolytic cleavage, required for mitochondrial fusion. Mutations in *AFG3L2* cause spinocerebellar ataxia type 28 and a complex neurodegenerative syndrome of childhood. In this study, we demonstrated that the loss of AFG3L2 in mouse embryonic fibroblasts (MEFs) reduces mitochondrial Ca^{2+} uptake capacity. This defect is neither a consequence of global alteration in cellular Ca^{2+} homeostasis nor of the reduced driving force for Ca^{2+} internalization within mitochondria, since cytosolic Ca^{2+} transients and mitochondrial membrane potential remain unaffected. Moreover, experiments in permeabilized cells revealed unaltered mitochondrial Ca^{2+} uptake speed in *Afg3l2*$^{-/-}$ cells, indicating the presence of functional Ca^{2+} uptake machinery. Our results show that the defective Ca^{2+} handling in *Afg3l2*$^{-/-}$ cells is caused by fragmentation of the mitochondrial network, secondary to respiratory dysfunction and the consequent processing of OPA1. This leaves a number of mitochondria devoid of connections to the ER and thus without Ca^{2+} elevations, hampering the proper Ca^{2+} diffusion along the mitochondrial network. The recovery of mitochondrial fragmentation in *Afg3l2*$^{-/-}$ MEFs by overexpression of OPA1 rescues the impaired mitochondrial Ca^{2+} buffering, but fails to restore respiration. By linking mitochondrial morphology and Ca^{2+} homeostasis, these findings shed new light in the molecular mechanisms underlining neurodegeneration caused by *AFG3L2* mutations.

INTRODUCTION

Mitochondria are interconnected dynamic organelles central to energy production, fatty acid metabolism and Ca^{2+} buffering. Dysfunction of mitochondria causes oxidative stress, perturbed cellular Ca^{2+} homeostasis and cell death and is linked to aging and neurodegeneration.

Several surveillance mechanisms have evolved to prevent the accumulation of dysfunctional mitochondria, such as the continuous remodelling of the mitochondrial network and mitophagy (1). At the organellar level, highly conserved proteases conduct protein quality control (2). Among them, *m*-AAA proteases belong to the AAA-protein superfamily (ATPases associated with a variety of cellular activities) and

*To whom correspondence should be addressed at: Vita-Salute San Raffaele University & Center for Translational Genomics and Bioinformatics, San Raffaele Scientific Institute, Via Olgettina 58, Milan, Italy. Tel: +39 0226433502; Fax: +39 0226436352; Email: casari.giorgio@hsr.it

are present as AFG3L2 homo-oligomers or paraplegin-AFG3L2 hetero-oligomers in the inner mitochondrial membrane. The *m*-AAA complexes mediate the selective degradation of non-assembled and damaged proteins (2) and exert chaperone-like activity on respiratory chain complexes (3–5). In addition, they perform proteolytic cleavage of substrates, which are the nuclear-encoded subunit of mitochondrial ribosomes MrpL32 and the regulator of mitochondrial fusion OPA1 (6,7). Both paraplegin and AFG3L2 have been linked to neurodegenerative disorders: mutations in the paraplegin-coding gene cause a recessive form of hereditary spastic paraplegia (8), while heterozygous and homozygous mutations in *AFG3L2* have been associated to spinocerebellar ataxia type 28 (SCA28) (9–11) and to a novel progressive myoclonic epilepsy-ataxia-polyneuropathy syndrome of childhood, respectively (12). Whether these diverse diseases reflect tissue-specific expression level of paraplegin and AFG3L2 (13) or different substrate specificity of the two proteases remain to be clarified.

We provided evidence that *Afg3l2*$^{-/-}$ mice resemble patients carrying homozygous mutations, showing a severe neurological syndrome that leads to lethality at P16 (5). Accordingly, *Afg3l2* haploinsufficient mice recapitulate most features of SCA28 patients, displaying defects in motor coordination and balance due to dark degeneration of Purkinje cells (PC-DCD) (14). The latter is a phenomenon documented in other SCAs as secondary to excitotoxicity and high levels of intracellular Ca^{2+}, which cause calpain-mediated cytoskeletal breakdown (15,16). Peculiarly, in the SCA28 model, PC-DCD originates from mitochondrial dysfunction, as demonstrated by the fact that alterations in mitochondrial morphology and metabolism precede PC degeneration (14).

We hypothesize that *Afg3l2*-depleted mitochondria have defective Ca^{2+} buffering capacity, leading to dysregulation of cytosolic Ca^{2+} homeostasis and finally to PC-DCD. Indeed, compelling evidence in the literature points at the central role of mitochondrial Ca^{2+} buffering in shaping the amplitude and the spatio-temporal dimension of intracellular Ca^{2+} waves (17,18). This is particularly crucial for neurons, and especially for PCs, which uniquely receive glutamatergic afferents and experience large and sudden Ca^{2+} influx (19).

Mitochondria take up Ca^{2+} rapidly from the cytoplasm during agonist-induced Ca^{2+} signals, thanks to the strong driving force ensured by the mitochondrial membrane potential ($\Delta\psi_m$) via a low-affinity Ca^{2+} channel of the inner membrane (20). Impairment of mitochondrial Ca^{2+} buffering can result from dysfunction of mitochondrial metabolism or from functional defects of the mitochondrial Ca^{2+} uptake machinery (20,21). Also, fragmentation of the mitochondrial network has been shown to interrupt intramitochondrial Ca^{2+} wave and to reduce mitochondrial Ca^{2+} uptake (22).

In this study, we investigated the mitochondrial Ca^{2+} handling capacity in *Afg3l2*- depleted fibroblasts. Our results demonstrate that the loss of AFG3L2 reduces the average mitochondrial Ca^{2+} uptake leaving $\Delta\psi_m$ and the Ca^{2+} import machinery unaffected. The defective Ca^{2+} load is caused by fragmentation of the mitochondrial network, due to increased processing of OPA1, which reduces the volume of individual organellar particles and disrupt the matrix continuity of the mitochondrial network.

RESULTS

Loss of *Afg3l2* causes reduced mitochondrial Ca^{2+} uptake

To examine the effect of the loss or haploinsufficiency of *Afg3l2* on mitochondrial Ca^{2+} buffering, we performed Ca^{2+} measurements on mouse embryonic fibroblasts (MEFs) by employing aequorin chimeras targeted to mitochondria and cytosol compartments (mtAEQmut and cytAEQ) (23). Cells were challenged with bradykinin, which leads to an inositol (1,4,5) triphosphate-triggered release of Ca^{2+} from the ER stores and its accumulation in the mitochondrial matrix. In *Afg3l2*$^{-/-}$ cells, the mitochondrial Ca^{2+} peak response ($[Ca^{2+}]_m$) elicited by bradykinin stimulation (50.71 $\pm$ 7.54 μM) was strongly reduced compared with *Afg3l2*$^{+/-}$ (74.47 $\pm$ 7.95 μM, $P < 0.001$) and wild-type cells (82.87 $\pm$ 10.79 μM, $P < 0.001$), as measured by the low-affinity mtAEQmut probe (Fig. 1A). The decreased mitochondrial Ca^{2+} response in *Afg3l2*$^{-/-}$ cells was specific of mitochondria and not secondary to global cellular Ca^{2+} signalling. In fact, cytosolic Ca^{2+} response ($[Ca^{2+}]_c$) measured by the cytAEQ probe after bradykinin stimulation revealed no alterations in *Afg3l2*$^{-/-}$ cells (1.52 $\pm$ 0.13 μM) compared with wild-type cells (1.52 $\pm$ 0.2 μM) (Fig. 1B). *Afg3l2*$^{+/-}$ cells showed a decreased $[Ca^{2+}]_c$ trend (1.35 $\pm$ 0.2 μM) that may explain the reduction in $[Ca^{2+}]_m$ (Fig. 1A).

We then verified whether the reduction in $[Ca^{2+}]_m$ in *Afg3l2*$^{-/-}$ cells was dependent on ER as Ca^{2+} source. We therefore induced capacitative Ca^{2+} entry to raise intracellular-free Ca^{2+} (24). We treated cells with thapsigargin, an irreversible inhibitor of the sarcoplasmic reticulum Ca^{2+}ATPase (SERCA pump), in the absence of extracellular Ca^{2+} to deplete ER stores and to activate store-operated Ca^{2+} channels at the plasma membrane. The re-addition of 1 mM Ca^{2+} resulted in comparable $[Ca^{2+}]_m$ responses in the three genotypes (1.65 $\pm$ 0.39 μM in the wild-type; 1.95 $\pm$ 0.43 in heterozygous and 1.74 $\pm$ 0.45 in *Afg3l2*$^{-/-}$ cells) (Fig. 1C). These experiments demonstrate that *Afg3l2* null mitochondria show decreased average $[Ca^{2+}]_m$ elevations in the presence of a maximal Ca^{2+}stimulation, as at the mouth of IP3 receptor channels (Fig. 1C).

Latent mitochondrial dysfunction of *Afg3l2*$^{-/-}$ MEFs in the presence of unaltered Ca^{2+} uptake speed and basal $\Delta\psi_m$

We next examined whether mitochondria of *Afg3l2*$^{-/-}$ cells have an intrinsic defect in Ca^{2+} accumulation by measuring mitochondrial Ca^{2+} uptake in digitonin-permeabilized cells and by imposing an ethylene glycol tetraacetic acid (EGTA)-buffered Ca^{2+} concentration of 2 μM (see Materials and Methods). In these conditions, all mitochondria are allowed to take up Ca^{2+} independently of their proximity to the Ca^{2+} source. The Ca^{2+} uptake speed, estimated by linear regression from the slope of the ascending phase of $[Ca^{2+}]_m$ rise (see Materials and Methods), was unchanged in *Afg3l2*$^{-/-}$ cells compared with syngenic controls (Fig. 2A). These data indicate that individual mitochondria lacking AFG3L2 have intact ability to internalize Ca^{2+}, meaning that the uptake machinery is likely not altered. We then directly verified the mRNA and protein levels of the mitochondrial

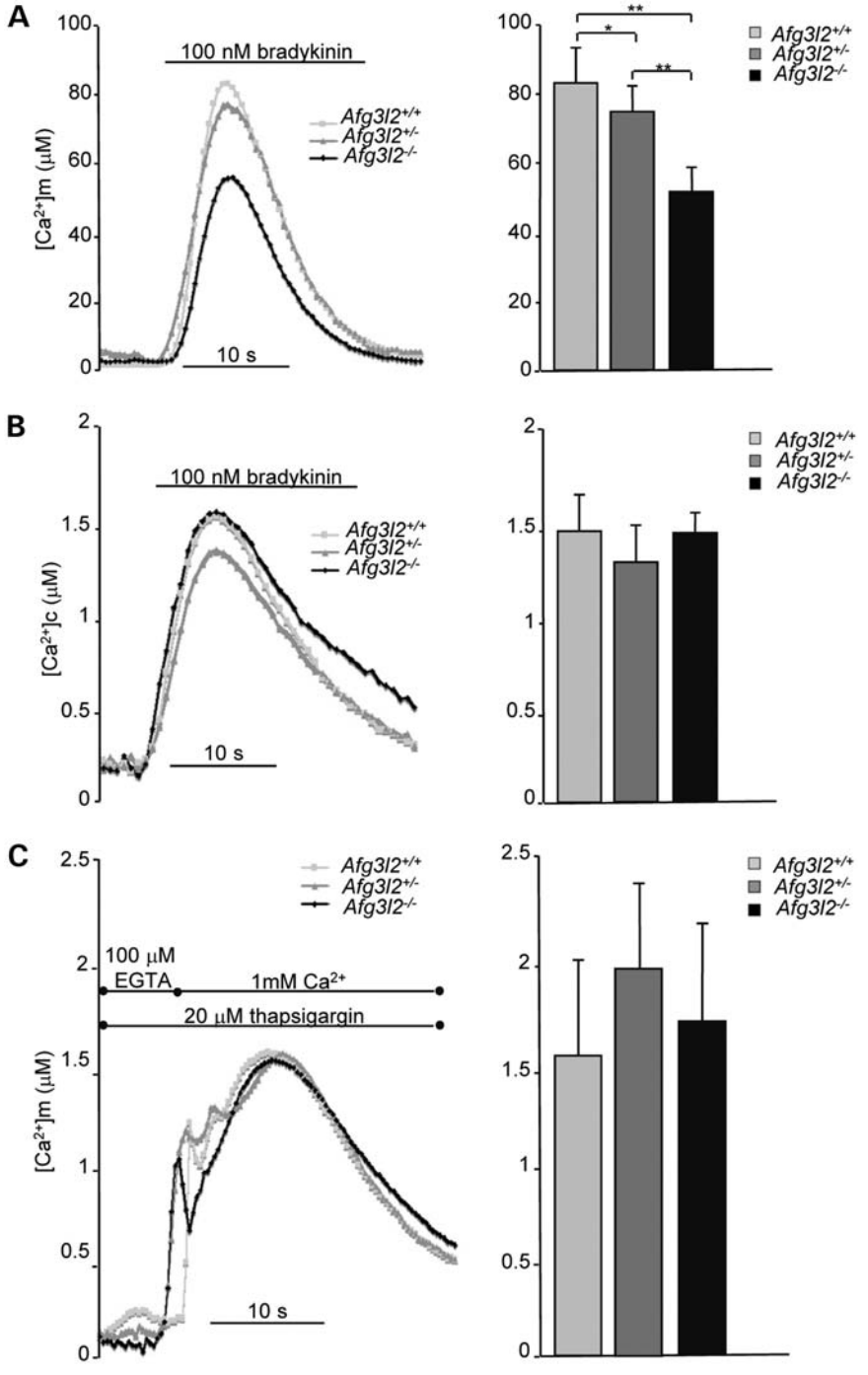

Figure 1. Loss of *Afg3l2* reduces mitochondrial Ca^{2+} uptake. (**A** and **B**) $[Ca^{2+}]_m$ and $[Ca^{2+}]_c$ in *Afg3l2* MEFs of the indicated genotypes measured by aequorin probes (mtAEQmut and cytAEQ). On the left: representative graphs; on the right: means ± SD of $[Ca^{2+}]_m$ and $[Ca^{2+}]_c$ peak responses after bradykinin stimulation, respectively (16 traces obtained from four independent experiments). Student's *t*-test: $^{**}P < 0.001$, $^{*}P < 0.05$. (**C**) Measurement of $[Ca^{2+}]_m$ (mtAEQ) after capacitative Ca^{2+} influx. On the left: representative graph; on the right: means ± SD of mitochondrial peak Ca^{2+} responses (10–12 traces obtained from four independent experiments).

Ca^{2+} uniporter (MCU) and of its regulator mitochondrial calcium uptake 1 (MICU1). Real-time qPCR revealed comparable levels of both transcripts in the three genotypes. Accordingly, western blot showed unchanged protein levels of MCU and MICU1 in *Afg3l2*$^{-/-}$ cells compared with controls (Fig. 2B).

Since mitochondrial Ca^{2+} uptake is dependent on $\Delta\psi_m$ and we previously reported respiratory defects in neuronal tissues from *Afg3l2* knockout and haploinsufficient mouse models (5,14), we tested whether the defective mitochondrial Ca^{2+} loading of *Afg3l2*$^{-/-}$ cells could be secondary to altered membrane polarization. The measurement of $\Delta\psi_m$ by the evaluation

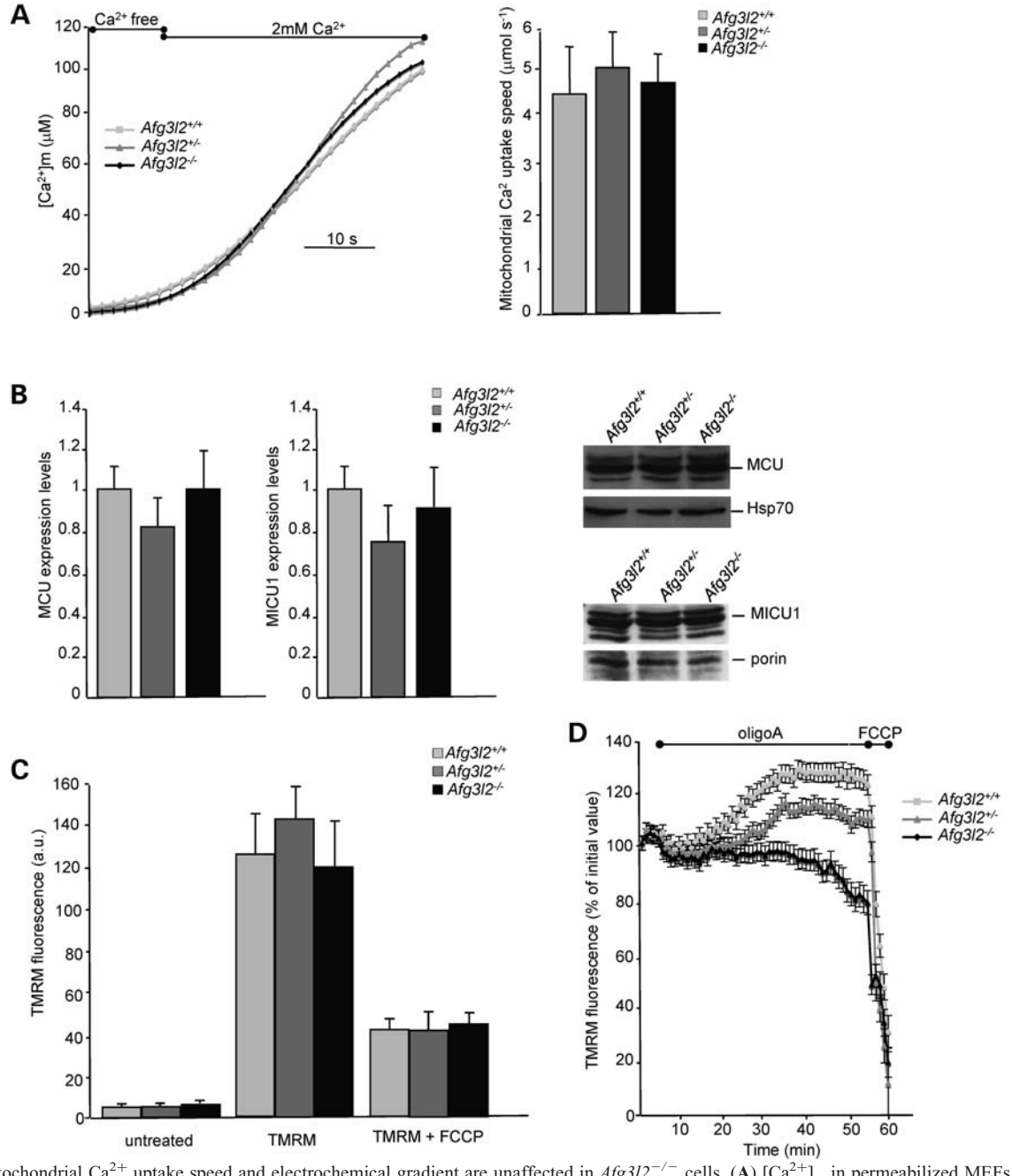

Figure 2. Mitochondrial Ca^{2+} uptake speed and electrochemical gradient are unaffected in *Afg3l2*$^{-/-}$ cells. (**A**) $[Ca^{2+}]_m$ in permeabilized MEFs measured by mtAEQmut. On the left: representative graph; on the right: means ± SD of the slope of $[Ca^{2+}]_m$ rise-ascending phase (10–12 traces obtained from four independent experiments). (**B**) On the right: quantification (real-time qPCR) of MCU and MICU1 mRNA relative to GAPDH mRNA (wild-type was set to 1). On the left: MCU and MICU1 immunoblot analysis of total cell extracts from *Afg3l2* MEFs of the indicated genotypes. Bars represent means ± SD of three independent experiments. (**C**) Analysis of $\Delta\psi_m$ by uptake of the potentiometric dye TMRM. TMRM fluorescence intensity in *Afg3l2*$^{-/-}$ MEFs and controls relative to unloaded cells was measured by cytofluorimetry. Bars represent means ± SD of four independent experiments. a.u.: arbitrary units. (**D**) Real-time imaging of TMRM fluorescence intensity of *Afg3l2*$^{+/+}$, *Afg3l2*$^{+/-}$ and *Afg3l2*$^{-/-}$ MEFs loaded with 20 nM TMRM. Cells were imaged every 60 s and mitochondrial TMRM fluorescence intensity was calculated as described. Where indicated, 4 μg/ml oligomycin A (OligoA) and 4 μM FCCP were added. Data represent mean ± SE of three independent experiments.

of the steady-state loading of the potentiometric dye tetramethyl rhodamine methyl ester (TMRM) into mitochondria of *Afg3l2*$^{-/-}$, *Afg3l2*$^{+/-}$ and wild-type MEFs revealed no differences in the three genotypes (Fig. 2C). From these data, we conclude that the reduced Ca^{2+} uptake ability of *Afg3l2*$^{-/-}$ cells is due neither to defective Ca^{2+} uptake machinery nor to a reduced driving force for Ca^{2+} influx.

Nevertheless, a latent mitochondrial dysfunction of *Afg3l2*$^{-/-}$ MEFs could be masked by the ATP synthase operating in the reverse mode and maintaining $\Delta\psi_m$ during the

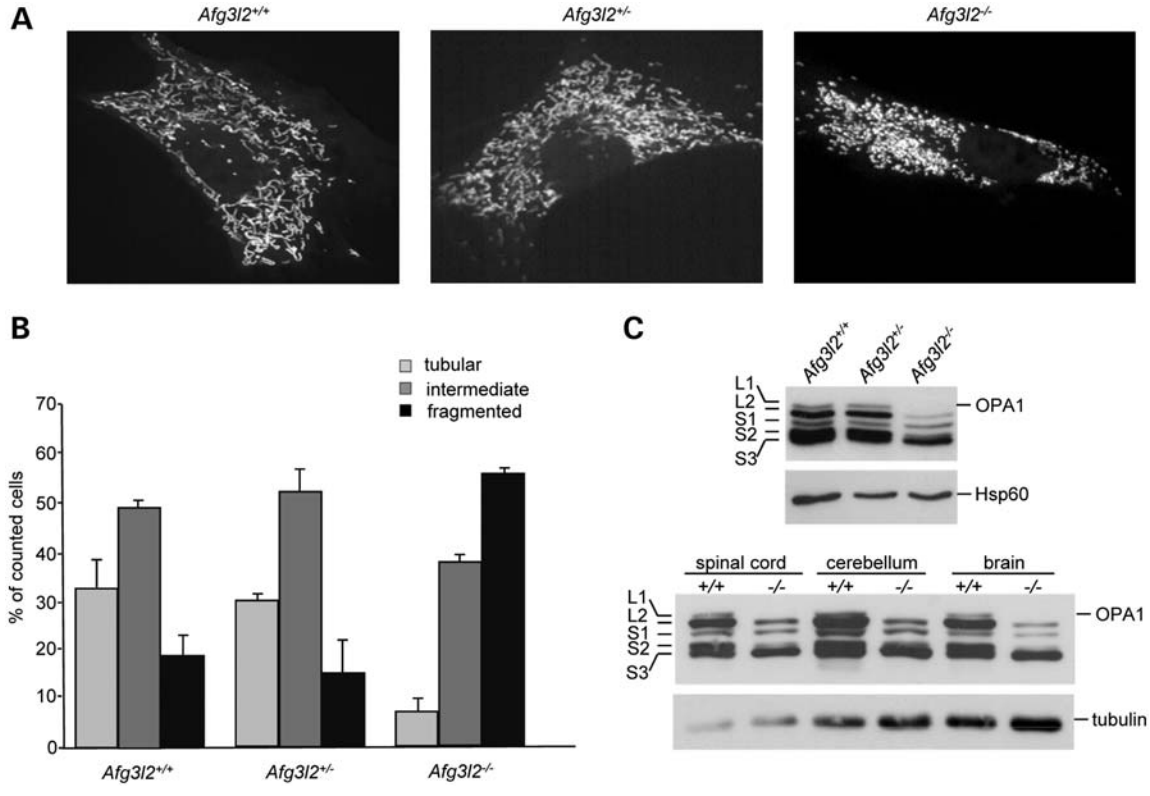

Figure 3. Increased mitochondrial fragmentation in *Afg3l2*$^{-/-}$ cells. (**A**) Representative pictures of mitochondrial morphology in *Afg3l2* MEFs transfected with mt-YFP and visualized by confocal microscopy. (**B**) Morphometric analysis of mitochondrial morphology in *Afg3l2* MEFs. One hundred and fifty randomly selected cells were analysed in each experiment. Bars represent means ± SD of three independent experiments. The Chi-squared test (2 degrees of freedom): *Afg3l2*$^{-/-}$ versus either heterozygous or wild-type MEFs = $P < 0.001$. (**C**) Immunoblot analysis of total cell extracts from *Afg3l2* MEFs (upper panel) or neuronal tissues of the indicated genotypes (lower panel). The five OPA1 bands are indicated as long (L1 and L2) and short isoforms (S1, S2 and S3) (30). Hsp60 and tubulin were used to verify equal loading, respectively.

experiment, a mechanism that has already been described in the literature (25). To test this hypothesis, we measured $\Delta\psi_m$ by real-time imaging of TMRM fluorescence intensity during incubation of cells with oligomycin A (OligoA), an inhibitor of mitochondrial F_1F_O-ATP synthase (25,26). As expected, addition of OligoA to healthy respiring cells like wild-type MEFs resulted in hyperpolarization of the inner membrane. In fact, protons pumped by the respiratory chain in the intermembrane space cannot cross the F_1F_O-ATP synthase and remain in the intermembrane space. In contrast, OligoA addition resulted in a mild mitochondrial hyperpolarization of *Afg3l2*$^{+/-}$ MEFs and in a slow but progressive mitochondrial depolarization in *Afg3l2*$^{-/-}$ cells, indicating that the maintenance of $\Delta\psi_m$ in *Afg3l2*$^{-/-}$ cells relies on the reverse activity of the ATP synthase (Fig. 2D).

To exclude that the drop of $\Delta\psi_m$ was secondary to the induction of the mitochondrial permeability transition (MPT), which depends on the opening of the permeability transition pore (PTP) (27), we performed real-time imaging of TMRM fluorescence pre-incubating the cells with a known inhibitor of MPT, cyclosporine A (CsA), that desensitizes the PTP via its mitochondrial receptor cyclophilin D (27). The treatment with CsA did not prevent the $\Delta\psi_m$ drop that is induced by OligoA in *Afg3l2*$^{-/-}$ MEFs, demonstrating that MPT is not occurring in these cells (data not shown).

Altogether, these data indicate that $\Delta\psi_m$ in *Afg3l2*$^{-/-}$ cells is not maintained by respiration but rather by a reverse activity of the F_1F_O-ATP synthase, which pumps protons from the matrix to the intermembrane space, thereby consuming ATP. This mechanism masks the mitochondrial dysfunction in *Afg3l2*$^{-/-}$ cells, in line with an impairment of the respiratory chain activity.

Afg3l2$^{-/-}$ cells show increased mitochondrial fragmentation

Alterations of mitochondrial shape may account for the inefficient mitochondrial Ca^{2+} handling of *Afg3l2*$^{-/-}$ cells. Indeed, it has been demonstrated that fragmentation of the mitochondrial network impairs mitochondrial Ca^{2+} uptake by modifying the spatial pattern of the intra-mitochondrial Ca^{2+} diffusion (22,28).

We thus evaluated the effect of the loss of *Afg3l2* on the regulation of mitochondrial network morphology by performing live imaging confocal microscopy in cells overexpressing a mitochondria-targeted yellow fluorescent protein (mt-YFP). Similarly to what reported by Ehses *et al*. (29) upon concomitant downregulation of both *Afg3l1* and *Afg3l2* in MEFs, we observed a marked alteration in mitochondrial network morphology in *Afg3l2*$^{-/-}$ cells. Morphometric analysis revealed that wild-type and heterozygous MEFs have

elongated and interconnected mitochondria. In contrast, *Afg3l2*$^{-/-}$ cells showed more than 50% of cells with small, round-shaped organelles and only 5% of cells with a tubular mitochondrial network (Fig. 3A and B).

The proper balance of long and short OPA1 isoforms is critical for maintenance of tubular mitochondrial morphology (30). MEFs express four alternative splicing mRNAs coding for OPA1 isoforms, resulting from the inclusion or the exclusion of exons 4b and 5b (31). These isoforms undergo different proteolytic cleavages (7,30,32) resulting in five bands on SDS–PAGE, corresponding to long (L1 and L2) and short (S1 to S3) processed OPA1 isoforms. The analysis of OPA1 band pattern in wild-type, *Afg3l2*$^{+/-}$ and *Afg3l2*$^{-/-}$ cells by western blotting revealed that the loss of AFG3L2 results in alteration of OPA1 processing: we detected an increased amount of short OPA1 forms and the almost-complete disappearance of the long bands in *Afg3l2*$^{-/-}$ MEFs (Fig. 3C). No apparent differences were observed between *Afg3l2* wild-type and heterozygous cells, indicating that AFG3L2 haploinsufficiency does not affect OPA1 processing and mitochondrial morphology in this cellular system (Fig. 3A–C). Mitochondrial fragmentation in *Afg3l2*$^{-/-}$ MEFs is rescued by the overexpression of wild-type AFG3L2, but this effect is not achieved with the overexpression of AFG3L2^{M666R}, one of the most severe SCA28-causing mutations (10) (Supplementary Material, Fig. S1A).

We also evaluated OPA1 processing in the neuronal tissues of *Afg3l2*$^{-/-}$ mice, in particular in the brain, cerebellum and spinal cord, which are the most affected by *Afg3l2* loss and also by *AFG3L2* mutations (5,10,12). As shown in the western blot in Figure 3C, OPA1 processing is increased in *Afg3l2*$^{-/-}$ mouse neuronal tissues, thus confirming the pathogenetic relevance of mitochondrial fragmentation in *AFG3L2*-associated diseases.

Fission of the mitochondrial network reduces organellar matrix continuity and leaves a fraction of mitochondria devoid of connection to the ER

We evaluated whether the mitochondrial fragmentation observed in *Afg3l2*$^{-/-}$ cells could impact on the number of mitochondria/ER contacts, specialized sites where IP3R/RyR-mediated Ca^{2+} oscillations are propagated locally to the mitochondria. The close vicinity of mitochondria to Ca^{2+}-release sites on the ER is crucial for the activation of the MCU and thus for the rapid and efficient accumulation of Ca^{2+} inside the organelles (33,34). To measure the total number of contacts in the whole cell volume, we analysed the colocalization between mitochondria and ER with three-dimensional (3D) reconstruction and volume rendering of confocal stacks of ER-targeted green fluorescent protein (ER-GFP) and mitochondrial-targeted red fluorescent protein (mt-RFP) in the three genotypes, as previously reported (22,35) (Fig. 4A). In this analysis, we considered the overlapping mitochondrial and ER spots as the sites where most-efficient Ca^{2+} transfer between the two organelles occurs, thus satisfying the high Ca^{2+} concentration demand for the opening of the MCU. As measured by Manders' colocalization coefficient (36), we found that the evident fragmentation of the mitochondrial network does not affect the average number of mitochondria-ER contact sites in *Afg3l2*$^{-/-}$ cells (Fig. 4B).

Similarly, the overall volume of the organellar network of both mitochondria and ER is unaffected by the loss of AFG3L2, as demonstrated by quantitative morphological imaging of the mitochondrial and ER networks by transfecting cells with mt-RFP or ER-GFP, respectively. After 3D reconstruction of confocal stacks, the images were analysed evaluating the total volume of the organellar network. ER architecture was unaffected by the loss of *Afg3l2*, appearing as an interconnected network of cisternae spanning the whole cellular volume. We also observed that fragmentation of the mitochondrial network does not alter either the mitochondrial or the ER total volume, the ratio of the two organellar volumes being comparable in the three genotypes (Fig. 4C). According to the observed fragmentation, we found a significant reduction in the average size of individual mitochondrial particle in *Afg3l2*$^{-/-}$ cells compared with controls (6.94 ± 2.3 versus $12.68 \pm 3.35\ \mu m^3$ in wild-type and $12.3 \pm 1.91\ \mu m^3$ in heterozygous cells, $P < 0.001$) (Fig. 4C). Having the three cell lines the same mitochondrial total volume, these data indicate that *Afg3l2*$^{-/-}$ cells have an increased number of individual mitochondria compared to wild-type and heterozygous cells. This hypothesis was verified by counting the total number of RFP-positive objects per cell, which is almost doubled in *Afg3l2*$^{-/-}$ cells compared with control cells, while the percentage of objects that are in contact with the ER is reduced (Fig. 4D). These data demonstrate that a significant number of *Afg3l2* null mitochondria lacks connections to the ER, and thus to Ca^{2+} sources, and therefore remains without significant $[Ca^{2+}]_m$ rises.

Rescue of mitochondrial fragmentation by OPA1 and MFN1 overexpression restores normal mitochondrial Ca^{2+} uptake in *Afg3l2*$^{-/-}$ cells

To validate our hypothesis, we decided to investigate whether rescue of mitochondrial fragmentation could ameliorate mitochondrial Ca^{2+} uptake in *Afg3l2*$^{-/-}$ cells. For this purpose, we generated wild-type, heterozygous and knockout MEF lines stably expressing wild-type OPA1 isoform1 (OPA1v1) or a mutant version of OPA isoform1 carrying a mutation within the GTP-binding domain (OPA1v1Q297V). By mimicking the GTP-bound form of OPA1, this mutant has been described as constitutively active and disassembly resistant form (37). In order to avoid strong overexpression of OPA1, being known that this can cause clustering of small mitochondria (38), we transfected cells with pMSCV-OPA1v1 or pMSCV-OPA1v1Q297V constructs, where OPA1 cDNA expression is under the control of the weak murine stem cell virus promoter.

As already reported by other groups in transient transfection experiments (37), the expression levels of exogenous OPA1v1 and OPA1v1Q297V revealed by western blot analysis were modest. We indeed detected a slight increase in the expected second (L2) and fifth bands (S3) in cells expressing OPA1v1 and OPA1v1Q297V compared with those transfected with the empty vector (EV) (Supplementary Material, Fig. S2B). Nevertheless, we observed that the moderate overexpression of OPA1v1 and OPA1v1Q297V clearly affects mitochondrial morphology in stable cell lines. In fact, morphometric analysis

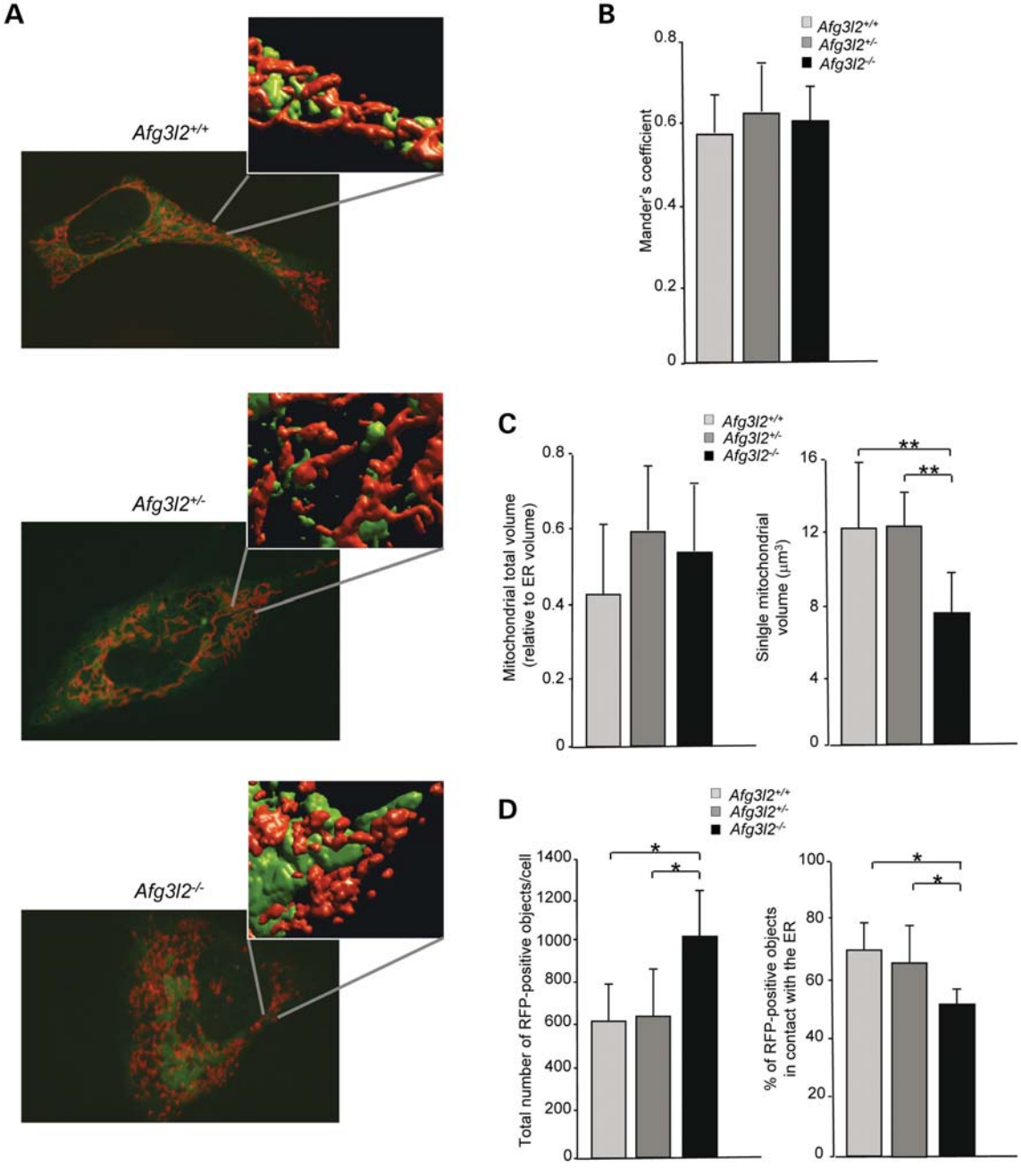

Figure 4. Mitochondrial fragmentation leaves a fraction of organelles free of connections to the ER. (**A**) Representative images of *Afg3l2* knockout, heterozygous and wild-type MEFs cotransfected with ER-GFP and mt-RFP. Insets show 3D reconstructed confocal stacks. (**B**) Quantitative analysis of ER-mitochondria colocalization estimated by Manders' coefficient. (**C**) Effect of *Afg3l2* depletion on total mitochondrial volume and on individual mitochondrial particles, respectively. (D) Quantification of the total number of RFP-positive objects and quantification of the percentage of RFP-positive objects in contact with the ER in the three genotypes. Data were obtained from an average of 60 randomly selected cells per genotype. Bars represent means ± SD of three independent experiments. Student's *t*-test: $^{*}P < 0.05$, $^{**}P < 0.001$.

revealed that >50% of the *Afg3l2*$^{-/-}$::EV analysed cells displayed fragmented mitochondria, exactly like immortalized *Afg3l2*$^{-/-}$ MEF$_S$. This percentage is strikingly reduced in *Afg3l2*$^{-/-}$::OPA1v1 cells, where most mitochondria appear in the intermediate state. The effect is even more evident in *Afg3l2*$^{-/-}$::OPA1v1Q297V MEFs, in which tubulated mitochondria are the most represented (Fig. 5A). Accordingly, imaging of *Afg3l2*$^{+/-}$::OPA1v1 cells revealed an increased percentage of tubular mitochondria compared with *Afg3l2*$^{+/-}$::EV cells. In *Afg3l2*$^{+/-}$::OPA1v1Q297V, most of the organelles are highly elongated and interconnected in a branched network (Supplementary Material, Fig. S3A and B). These findings indicate that the modest restoration of OPA1 L2 band is able to rescue mitochondrial fragmentation in *Afg3l2*$^{-/-}$ cells and to increase the fusion rate in *Afg3l2*$^{+/-}$ cells.

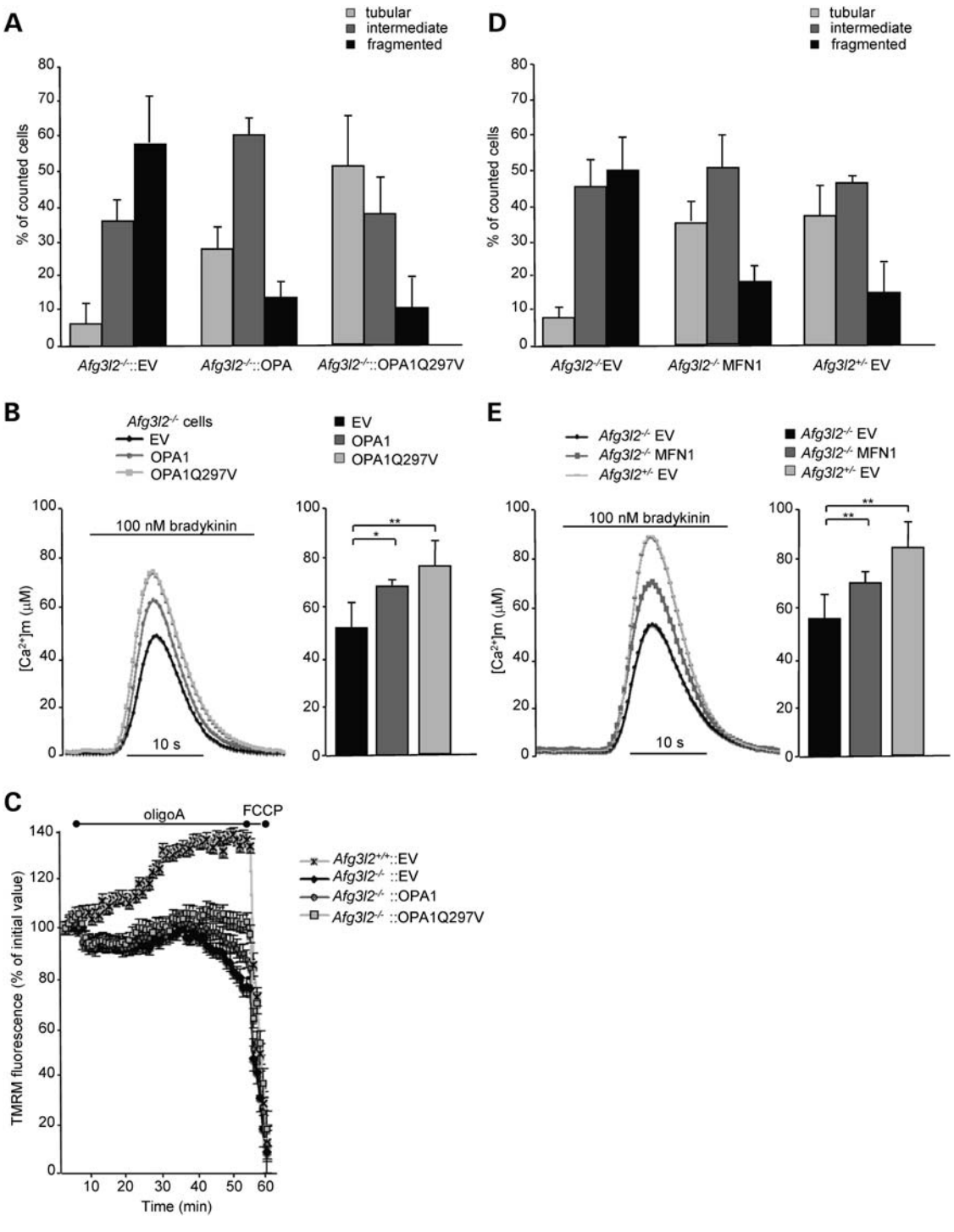

Figure 5. The defective mitochondrial Ca^{2+} uptake is rescued by OPA1 or MFN1 overexpression. (**A**) Morphometric analysis of mitochondrial morphology of *Afg3l2*$^{-/-}$ cells stably expressing wild-type OPA1v1 or OPA1v1-Q297V. One hundred and fifty randomly selected cells were analysed in each experiment. Bars represent means ± SD of three independent experiments. EV, empty vector. The Chi-squared test (2 degrees of freedom): *Afg3l2*$^{-/-}$::EV MEFs versus either ::OPA1v1 or ::OPA1v1Q297V = $P < 0.001$, ::OPA1v1 versus ::OPA1v1Q297V = $P < 0.001$. (**B**) $[Ca^{2+}]_m$ measured by aequorin probes (mitAEQmut) of *Afg3l2*$^{-/-}$ cells stably expressing wt OPA1v1 or OPA1v1-Q297V. On the left: representative graphs; on the right: means ± SD of $[Ca^{2+}]_m$ peak responses after bradykinin stimulation (12 traces obtained from four independent experiments). Student's *t*-test: $^{**}P < 0.001$, $^{*}P < 0.05$. (**C**) Real-time imaging of TMRM fluorescence intensity of *Afg3l2*$^{+/-}$ and *Afg3l2*$^{-/-}$ cells stably expressing wt OPA1v1 or OPA1v1-Q297V loaded with 20 nM TMRM. Cells were imaged every 60 s and mitochondrial TMRM fluorescence intensity was calculated as described. Where indicated, 4 μg/ml oligomycin A (OligoA) and 4 μM FCCP were added. Data represent mean ± SE of five independent experiments. (**D**) Morphometric analysis of mitochondrial morphology of *Afg3l2*$^{-/-}$ overexpressing MFN1. One hundred and fifty randomly selected cells were analysed in each experiment. Bars represent means ± SD of three independent experiments. The Chi-squared test (2 degrees of freedom): *Afg3l2*$^{-/-}$::EV MEFs versus either ::MFN1 or *Afg3l2*$^{+/-}$::EV = $P < 0.001$, *Afg3l2*$^{+/-}$::EV versus *Afg3l2*$^{-/-}$::MFN1 = $P < 0.001$. (**E**) $[Ca^{2+}]_m$ measured by aequorin probes (mitAEQmut) of *Afg3l2*$^{-/-}$ cells transfected with MFN1. On the left: representative graphs; on the right: means ± SD of $[Ca^{2+}]_m$ peak responses after bradykinin stimulation (10 traces obtained from two independent experiments). Student's *t*-test: $^{**}P < 0.001$.

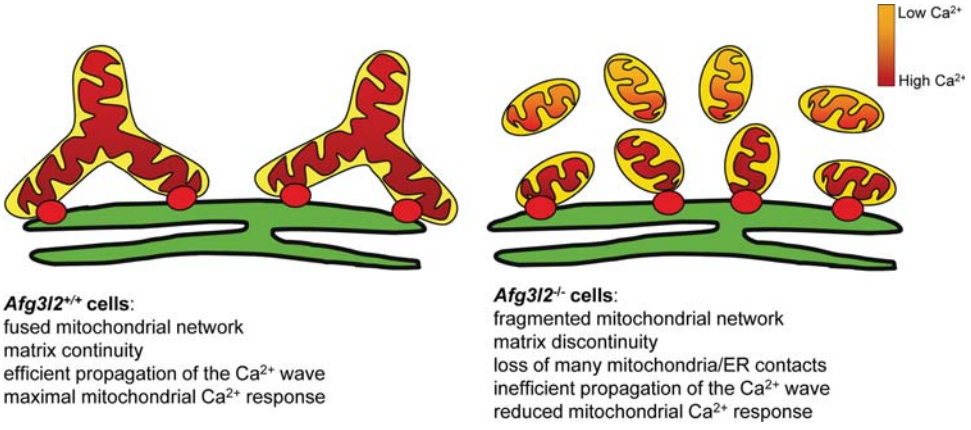

Figure 6. Model explaining the defective Ca^{2+} buffering in *Afg3l2*$^{-/-}$ cells. The red dots represent ER-mitochondria Ca^{2+} transmission sites. In *Afg3l2*$^{-/-}$ cells, many mitochondria remain without contacts with ER, and thus without Ca^{2+} elevations. The Ca^{2+} ions reaching mitochondria propagate less efficiently in a fragmented organellar network compared with a tubular one.

We next examined whether the rescue of mitochondrial morphology could ameliorate the defective Ca^{2+} handling capacity of *Afg3l2*$^{-/-}$ cells. We thus measured mitochondrial Ca^{2+} uptake in stable cell lines using the mitochondria-targeted aequorin mtAEQmut. Bradykinin stimulation of *Afg3l2*$^{-/-}$::EV MEFs resulted in $[Ca^{2+}]_m$ rises similar to those measured in *Afg3l2*$^{-/-}$ MEFs (51.46 ± 10.48 μM). On the contrary, OPA1v1 overexpressing cells showed a significant increase in the bradykinin-evoked $[Ca^{2+}]_m$ rise (66.7 ± 4.4 μM, $P < 0.05$), that was greater in OPA1v1Q297V overexpressing cells (76.1 ± 9.1 μM, $P < 0.001$) (Fig. 5B).

To verify that the rescue of the defective Ca^{2+} uptake in *Afg3l2*$^{-/-}$::OPA1v1 and *Afg3l2*$^{-/-}$::OPA1v1Q297V was specifically caused by the recovery of mitochondrial morphology and not by a different effect of OPA1 overexpression in the inner membrane, we tested whether it can be achieved by stimulating mitochondrial fusion through a different molecular system. Namely, we assessed mitochondrial morphology in *Afg3l2*$^{-/-}$ cells after overexpression of MFN1, essential for outer membrane fusion (39), and we observed a significant reduction in the amount of cells harbouring fragmented organelles and an increased quote of cells harbouring fused organelles (Fig. 5D). Of note, we found that MFN1 overexpression is able to increase bradykinin-evoked $[Ca^{2+}]_m$ rise in *Afg3l2*$^{-/-}$ MEFs (68.61 ± 4.3 μM, $P < 0.001$) compared with mock-transfected cells (55.49 ± 9.18 μM) (Fig. 5E). These data prove that *Afg3l2*$^{-/-}$ cells are still fusion competent and clearly demonstrate that the defective ability of *Afg3l2*$^{-/-}$ cells to internalize Ca^{2+} is dependent on fragmentation of the mitochondrial network (Fig. 6).

Since stable expression of OPA1v1 or OPA1v1-Q297V rescued the mitochondrial network fragmentation in *Afg3l2*$^{-/-}$ MEFs, we then examined whether OPA1 can rescue also the progressive mitochondrial depolarization of OligoA-treated *Afg3l2*$^{-/-}$ MEFs. The real-time imaging of TMRM in these stable cell lines exposed to OligoA showed no recovery of the $\Delta\psi_m$ in *Afg3l2*$^{-/-}$ cells stably expressing wild-type OPA1v1 or OPA1v1-Q297V to levels comparable to the control cells (Fig. 5C). Therefore, we conclude that the rescue of mitochondrial network morphology by OPA1 is not sufficient to recover the latent mitochondrial dysfunction of *Afg3l2*$^{-/-}$ cells.

DISCUSSION

In this study, we evaluated the mitochondrial Ca^{2+} uptake capacity of *Afg3l2*-depleted cells. Our results show that the loss of *Afg3l2* causes a marked reduction in mitochondrial Ca^{2+} buffering. This defect depends neither on impaired organellar Ca^{2+} uptake machinery nor on alteration of $\Delta\psi_m$, since MCU mRNA and protein levels and TMRM loading resulted comparable between mutant and controls. These observations are in line with the fact that *Afg3l2*$^{-/-}$ individual mitochondria present intact ability to accumulate Ca^{2+}, as demonstrated by unchanged Ca^{2+} uptake speed in digitonin-permeabilized cells experiments. We showed that the defective Ca^{2+} uptake of *Afg3l2*$^{-/-}$ cells is instead caused by fragmentation of the mitochondrial network, secondary to enhanced processing of OPA1. Evidence for this mechanism is provided by rescue experiments, where we stably expressed wild-type OPA1v1 or a constitutively active form of OPA1 (OPA1v1-Q297V) in *Afg3l2*$^{-/-}$ MEFs. By slightly increasing the amount of the long OPA1 isoforms (L2 band) that promote organellar fusion, the overexpression of OPA1v1 is able to recover fragmentation of the mitochondrial network in *Afg3l2*$^{-/-}$ cells. This effect is even more pronounced with OPA1v1-Q297V overexpression, which increases the number of cells with a tubular network, besides reducing mitochondrial fragmentation. This can be explained by the fact that Q297V mutation, as previously proposed (37,40), should make OPA1 constitutively active by mimicking the GTP-bound state. Notably, we showed that fusion restoration in *Afg3l2*$^{-/-}$::OPA1v1 MEFs significantly ameliorates mitochondrial Ca^{2+} buffering respect to *Afg3l2*$^{-/-}$::EV cells and that the defect is completely recovered in *Afg3l2*$^{-/-}$::OPA1v1Q297V MEFs. We also demonstrated that overexpression of MFN1, an outer membrane regulator of mitochondrial fusion, exerts the same effect of OPA1v1 on both mitochondrial morphology and Ca^{2+} buffering in *Afg3l2*$^{-/-}$ MEFs.

These findings prove that mitochondrial fusion can occur in the absence of AFG3L2 and can be enhanced by overexpressing mitochondrial fusion regulators. In addition, since MFN1 can efficiently tubulate mitochondria in the presence of OPA1 (38), they indicate that the overall amount of long and short OPA1 isoforms present in *Afg3l2*-depleted cells is sufficient to respond to fusion induction triggered by MFN1. Moreover, these data demonstrate that impaired Ca^{2+} buffering in the absence of AFG3L2 is indeed caused by mitochondrial fragmentation secondary to enhanced OPA1 processing.

The mechanism through which the loss of AFG3L2 induces increased processing of OPA1 is not fully understood. OMA1, a metallopeptidase of the inner mitochondrial membrane, mediates the cleavage of OPA1 in the absence of AFG3L2 (29). Moreover, the loss of $\Delta\psi_m$ or decreased ATP levels is known to augment OPA1 processing (41,42). Whether OMA1 is directly regulated by AFG3L2 itself or indirectly by the respiratory deficiencies mediated by the loss of AFG3L2 (5) remains to be determined. Here, we provide evidence that respiratory dysfunction is the primary defect following AFG3L2 depletion and associates to mitochondrial fragmentation.

In fact, our studies on the regulation of $\Delta\psi_m$ in the absence of AFG3L2 in MEFs show that $\Delta\psi_m$ in basal conditions is not altered. On the other hand, treatment with the ATP-synthase inhibitor Oligo A revealed depolarization in *Afg3l2*$^{-/-}$ cells, indicating that $\Delta\psi_m$ is maintained through the reverse activity of the F_1F_O-ATP synthase and not by respiration. This phenotype is in line with a dysfunction in the activity of the respiratory chain complexes, which affects proton pumping across the inner mitochondrial membrane and requires reversion of the activity of ATP synthase (i.e. consuming ATP) for proton pumping from the matrix to the intermembrane space to achieve the maintenance of $\Delta\psi_m$. As a direct consequence, the inhibition of the ATP synthase activity by Oligo A produces a decline of $\Delta\psi_m$, as observed in *Afg3l2* knockout MEFs. Interestingly, stable expression of OPA1v1 or OPA1v1-Q297V is not able to rescue the progressive mitochondrial depolarization of OligoA-treated *Afg3l2*$^{-/-}$ MEFs to levels comparable with the wild-type demonstrating that the rescue of mitochondrial network morphology is not sufficient to recover the latent mitochondrial dysfunction. These data indicate that the impaired mitochondrial respiration is the primary defect following depletion of *Afg3l2* that we hypothesize is the cause of the increase in OPA1 processing and of the following mitochondrial fragmentation.

This is in line with the fact that in *Afg3l2*$^{+/-}$ MEFs, OligoA addition resulted in a milder hyperpolarization compared with wild-type cells. This can indicate a reduced efficiency of mitochondrial respiration in *Afg3l2*$^{+/-}$ cells, although mitochondrial morphology and OPA1 processing are not affected in this cellular system.

All this considered, we demonstrate the consequential arrangement of events, starting from loss of AFG3L2, to respiratory dysfunction, OPA1 cleavage and finally to organellar fragmentation, although some mechanistic steps of this process are indeed still lacking and maybe include some new effectors still to be identified.

We observed that mitochondrial fragmentation in *Afg3l2*$^{-/-}$ cells reduces the volume of individual mitochondrial particles without changing the total volume of the organellar network. As a direct consequence, a fraction of mitochondria in *Afg3l2*$^{-/-}$ cells lose their link to the ER and result positioned at a higher distance from the Ca^{2+} source, failing to match the MCU-activation needs (33) and therefore remaining without substantial $[Ca^{2+}]_m$ rises. Moreover, studies have shown that Ca^{2+} entering mitochondria can spread and equilibrate rapidly within the matrix along large and tubular, but not fragmented organelles. In fact, the small size of mitochondrial particles in a fragmented network and the consequent lack of matrix connectivity limit the proper diffusion of the Ca^{2+} wave and increases the heterogeneity of mitochondrial Ca^{2+} responses (22,28). Together, these phenomena account for the overall reduction in the mitochondrial Ca^{2+} load in *Afg3l2*$^{-/-}$ cells.

Heterozygous and homozygous mutations in *AFG3L2* cause neurodegeneration that involves PCs in the cerebellum and results in ataxia (9,12). The fact that cerebellum is more sensitive to AFG3L2 dysfunction compared with other neuronal tissues can be explained by the high expression of this gene in PCs (9), but also with the special requirement of mitochondrial functionality by PCs. These are indeed unique neurons with very large and highly branched dendritic trees that receive only excitatory inputs. They are therefore exposed to high Ca^{2+} influxes due to glutamatergic stimulation of both mGluR1 and AMPA receptors (19). For these reasons, mitochondria play a pivotal role in maintaining Ca^{2+} homeostasis in PCs by direct uptake of Ca^{2+} and, also, by providing ATP to pump Ca^{2+} across membranes.

We therefore hypothesize that the inefficient buffering and shaping of the Ca^{2+} waves operated by mutant mitochondria provokes a local increase in $[Ca^{2+}]_c$ and that this, in chronic conditions like as in *AFG3L2*-associated diseases, triggers PCs degeneration.

Considering what mentioned above, it is conceivable that *Afg3l2* haploinsufficiency causes inefficient Ca^{2+} buffering in PCs in a progressive degenerative situation. Nonetheless, we failed to demonstrate mitochondrial fragmentation and defective Ca^{2+} uptake in *Afg3l2*$^{+/-}$ fibroblasts likely because in culture they rely marginally on mitochondria for ATP production and Ca^{2+} buffering compared with neurons and, also, because in these cells the Ca^{2+} wave could only be elicited by ER stimulation. Moreover, we performed acute experiments that do not properly mimic the physio-pathological condition of chronic degeneration.

We can hypothesize that fragmentation of the mitochondrial network in *Afg3l2*-depleted PCs causes defective mitochondrial Ca^{2+} buffering, but also inefficient trafficking of the organelles to dendritic stalks and distal branches. Indeed, it has been demonstrated that in PCs lacking mitochondrial fusion, both increased mitochondrial diameter due to swelling and aggregations of mitochondria seem to block efficient entry into neurites, resulting in a dearth of mitochondria in axons and dendrites (43). In the worst scenario, the two events may negatively synergize causing not only the inefficient opposition to Ca^{2+}wave close to the ER and at in dendrites, but the increased mitochondria retention in the cell soma, too.

In conclusion, our results functionally link for the first time AFG3L2 to mitochondrial Ca^{2+} buffering. The molecular pathogenesis of SCA28 can now be drawn in the light of the

inefficient mitochondrial Ca^{2+} uptake as one of the triggering events of PC-DCD.

MATERIALS AND METHODS

MEF lines

Primary MEFs were established from embryonic day E16.5 from *Afg3l2* knockout, heterozygous and wild-type embryos (5) and immortalized by SV40 (44), using 300 μg/ml geneticin for selection.

For the generation of stable cell lines, MEF_S were transfected with pMSCV-EV, pMSCV-OPA1v1 and pMSCV-OPA1v1Q297V constructs and selected with 1 μg/ml puromycin for 2 weeks. Transfection was performed using Metafectene (Biontex Laboratories, San Diego, CA, USA) according to the manufacturer's instruction.

Aequorin measurements

MEFs grown on 13 mm round glass cover slips at 50% confluence were transfected with the cytosolic (cytAEQ) or mitochondrial aequorin probes (mtAEQmut or mtAEQ). Cells were reconstituted with 5 μm coelenterazine for 90 min in DMEM supplemented with 1% fetal bovine serum, incubated in KRB (Krebs–Ring modified buffer: 125 mm NaCl, 5 mm KCl, 1 mm Na_3PO_4, 1 mm $MgSO_4$, 5.5 mm glucose, 20 mm 4-(2-hydroxyethyl)-1-piperazineethanesulfonic acid (HEPES), pH 7.4, 37°C) supplemented with 1 mm $CaCl_2$ and then transferred to the perfusion chamber. When indicated, 100 nm bradykinin was added. The experiments were concluded by lysing MEFs with 100 μm digitonin in a hypotonic Ca^{2+}-rich solution (10 mm $CaCl_2$ in H_2O), thus discharging the remaining aequorin pool. The light signal was collected in a purpose-built luminometer as previously described (23).

$[Ca^{2+}]_{mt}$ following capacitative Ca^{2+} influx was measured by perfusing MEFs with the SERCA inhibitor thapsigargin (1 μm) in a KRB solution containing no Ca^{2+} and 100 μm EGTA. Mitochondrial Ca^{2+} uptake was evoked by adding 1 mm $CaCl_2$ to the medium and was measured by mtAEQ.

In the experiments with permeabilized cells, a buffer mimicking the cytosolic Ca^{2+} ionic composition (intracellular buffer) was used: 130 mm KCl, 10 mm NaCl, 2 mm K_2HPO_4, 5 mm succinic acid, 5 mm malic acid, 1 mm $MgCl_2$, 20 mm HEPES, 1 mm pyruvate, 0.5 mm ATP and 0.1 mm ADP (37°C, pH 7). Intracellular buffer was supplemented with either 100 μm EGTA (intracellular buffer/EGTA) or a 2 mm EGTA and 2 mm hydroxy-2-ethylenediaminetriacetic acid-buffered $[Ca^{2+}]$ of 2 μm (intracellular buffer/Ca^{2+}) calculated with the Chelator software (45).

RNA extraction and gene expression analysis

Total RNA from cells was purified using Trizol (Invitrogen, Carlsbad, CA, USA) following the manufacturer's instructions. cDNA was generated using a Thermo script RT–PCR system kit (Invitrogen). For the expression of MCU and MICU1, cDNA was analysed by real-time PCR using the SYBR green chemistry (Light cycler 480, SYBR green I master, Roche, Basel, Switzerland). MCU and MICU1-PCR-primer sequences were previously described by De Stefani *et al*. (20). glyceraldehyde 3-phosphate dehydrogenase was used for normalization.

Western blot analysis

OPA1 band pattern was analysed by standard western blot procedure. Total cell lysate was prepared by protein extraction using a Triton-containing buffer (10 mm Tris–HCl, pH 7.4, 150 mm NaCl, 1% Triton, 1 mm ethylenediaminetetraacetic acid (EDTA) pH 8, 1X Protease Inhibitor Cocktail, Roche, Basel, Switzerland). Twenty micrograms of protein extracts were dissolved in sample buffer (60 mm Tris–HCl, pH 6.8, 5% glycerol, 1.7% SDS, 0.1 m DTT, 0.002% bromophenol blue), were separated on 7% SDS–PAGE and analysed by standard immunoblotting procedures. Anti-OPA1 antibody was from BD Transduction Laboratories (Franklin Lakes, NJ, USA), anti-Hsp60 and Hsp70 antibodies were from Stressgen (San Diego, CA, USA). For the detection of MCU and MICU1, cells were lysed with radio immunoprecipitation assay buffer (NaCl 150 mm, Tris–HCl 50 mm, EDTA 1 mm, pH 8, NP40 1%, SDS 0.1%, Sodium Deoxycholate 1%). Fifty micrograms of protein extracts were dissolved in sample buffer and loaded on a 7% SDS–PAGE followed by immunoblotting. Anti-MCU (CCDC109A) and anti-MICU1 antibodies were from SIGMA (St Louis, Missouri, USA), anti-tubulin was from Invitrogen.

Measurements of mitochondrial membrane potential

$\Delta\Psi_m$ was measured using the mitochondrial potentiometric dye TMRM (Invitrogen) and analysing cells uptake of the compound cytofluorimetrically. Cells were seeded in six-well multi-dishes, 300 000 cells/well. Twenty-four hours after plating, cells were collected, washed in PBS 1× and then suspended in phenol-red free Hank's buffered salt solution (HBSS) 1× supplemented with 10 mm HEPES, 2 μm Ciclosporin H (Alexis Biochemicals, San Diego, CA, USA) and 20 nm TMRM and incubated for 30 min at 37°C. In parallel, after incubation with TMRM containing medium, cells were treated for 5 min with 4 μm trifluorocarbonylcyanide phenylhydrazone (FCCP), as control of specific mitochondrial staining. TMRM fluorescence was analysed using Cytomics FC500 Flow Cytometry System (Beckman Coulter). Output files were analysed using flow cytometry data analysis program WinMDI 2.8.

Real-time analysis of $\Delta\psi_m$ was performed as follows. $Afg3l2^{+/+}$, $Afg3l2^{+/-}$ and $Afg3l2^{-/-}$ MEFs were plated in 12-well multi-dishes, 50 000 cells/well. After 40 h, cells were incubated with 20 nm TMRM, 2 μm CsH and 2 μg/ml Hoechst 33 342 dissolved in phenol-red free HBSS 1× supplemented with 10 mm HEPES for 30 min at 37°C. For CsA pretreatment, cells were incubated for 30 min at 37°C in the abovementioned medium supplemented with 2 μm CsA. Images were acquired with IN Cell Analyzer 1000 (GE Healthcare, Little Chalfont, UK). Sequential images of TMRM fluorescence from at least three regions of interest (ROIs) were acquired every 60 s. Four micrograms per millilitre oligomycin A and 4 μm FCCP were added in each well, after minute 5 and minute 55 of the acquisition, respectively, by In Cell Analyzer motorized injector. Images were stored for subsequent analysis using IN Cell Investigator software. Five

independent experiments were performed. The average TMRM fluorescence intensity of at least 15 ROIs minus background was calculated for each frame and normalized for comparative purposes.

Imaging analyses

Analysis of mitochondrial network morphology was performed as described (38) by expressing a mt-YFP (Clontech, Mountain View, CA, USA) and live imaging confocal microscopy. An average of 150 cells was analysed for each experimental condition. Cells were divided into three classes accordingly to mitochondria shape: tubular mitochondrial network, intermediate or fragmented mitochondrial structures. Experiments were repeated at least three times, and three operators analysed the images, independently. The Chi-squared test on row data was applied for significance calculation (degrees of freedom = 2).

For the analysis of mitochondrial and ER volumes, cells were transfected with mitochondrial-targeted red fluorescent protein mt-RFP (Clontech) and ER-targeted green fluorescent protein (ER-GFP, kindly provided by R. Sitia) and stacks of consecutive confocal images taken at 0.1 μm intervals were acquired. 3D reconstruction and volume rendering were performed using Volocity 3D Image Analysis Software version 5.5.1, Perkin Elmer, Norwalk, MA, USA.

Manders' coefficient was applied for the quantitative analysis of mitochondria-ER colocalization. In all the experiments, confocal microscopy was performed using Perkin Elmer UltraVIEW Spinning Disk Confocal Microscope and EMCCD Hamamatsu C9100 imaging camera. The system is equipped with a stage incubator from OkoLab (www.okolab.com), allowing to work with live cells maintained under stable conditions of temperature, CO_2 and humidity.

For each cell, the total number of red objects (mitochondria) was identified using the IN Cell Developer Toolbox 1.8 (GE Healthcare). After the optimization of segmentation parameters, a mask was created to cover the mitochondrial network. This mask was projected on the ER. At this point, a threshold was set in order to classify mitochondria using the green (ER) intensity. Mitochondria with a green signal intensity greater than or equal to the threshold were classified as in contact with the ER, whereas mitochondria with a green signal intensity less than threshold were classified as free of contacts.

SUPPLEMENTARY MATERIAL

Supplementary Material is available at *HMG* online.

ACKNOWLEDGEMENTS

We thank our internal imaging facility ALEMBIC and, in particular, Miriam Ascagni for technical assistance on real-time analysis of $\Delta\psi_m$ and for organelle quantification. We thank Riccardo Vago for FACS analysis technical assistance.

Conflict of Interest statement. None declared.

FUNDING

This work has been supported by the Italian Telethon Foundation (GGP 08138), Compagnia di San Paolo (Turin, Italy) and National Ataxia Foundation (Minneapolis, MN-USA). Funding to pay the Open Access publication charges for this article was provided by the Italian Telethon Foundation.

REFERENCES

1. Tatsuta, T. and Langer, T. (2008) Quality control of mitochondria: protection against neurodegeneration and ageing. *EMBO J.*, **27**, 306–314.
2. Koppen, M. and Langer, T. (2007) Protein degradation within mitochondria: versatile activities of AAA proteases and other peptidases. *Crit. Rev. Biochem. Mol. Biol.*, **42**, 221–242.
3. Arlt, H., Steglich, G., Perryman, R., Guiard, B., Neupert, W. and Langer, T. (1998) The formation of respiratory chain complexes in mitochondria is under the proteolytic control of the m-AAA protease. *EMBO J.*, **17**, 4837–4847.
4. Atorino, L., Silvestri, L., Koppen, M., Cassina, L., Ballabio, A., Marconi, R., Langer, T. and Casari, G. (2003) Loss of m-AAA protease in mitochondria causes complex I deficiency and increased sensitivity to oxidative stress in hereditary spastic paraplegia. *J. Cell Biol.*, **163**, 777–787.
5. Maltecca, F., Aghaie, A., Schroeder, D.G., Cassina, L., Taylor, B.A., Phillips, S.J., Malaguti, M., Previtali, S., Guenet, J.L., Quattrini, A. *et al.* (2008) The mitochondrial protease AFG3L2 is essential for axonal development. *J. Neurosci.*, **28**, 2827–2836.
6. Nolden, M., Ehses, S., Koppen, M., Bernacchia, A., Rugarli, E.I. and Langer, T. (2005) The m-AAA protease defective in hereditary spastic paraplegia controls ribosome assembly in mitochondria. *Cell*, **123**, 277–289.
7. Ishihara, N., Fujita, Y., Oka, T. and Mihara, K. (2006) Regulation of mitochondrial morphology through proteolytic cleavage of OPA1. *EMBO J.*, **25**, 2966–2977.
8. Casari, G., De Fusco, M., Ciarmatori, S., Zeviani, M., Mora, M., Fernandez, P., De Michele, G., Filla, A., Cocozza, S., Marconi, R. *et al.* (1998) Spastic paraplegia and OXPHOS impairment caused by mutations in paraplegin, a nuclear-encoded mitochondrial metalloprotease. *Cell*, **93**, 973–983.
9. Di Bella, D., Lazzaro, F., Brusco, A., Plumari, M., Battaglia, G., Pastore, A., Finardi, A., Cagnoli, C., Tempia, F., Frontali, M. *et al.* (2010) Mutations in the mitochondrial protease gene AFG3L2 cause dominant hereditary ataxia SCA28. *Nat. Genet.*, **42**, 313–321.
10. Cagnoli, C., Stevanin, G., Brussino, A., Barberis, M., Mancini, C., Margolis, R.L., Holmes, S.E., Nobili, M., Forlani, S., Padovan, S. *et al.* (2010) Missense mutations in the AFG3L2 proteolytic domain account for approximately 1.5% of European autosomal dominant cerebellar ataxias. *Hum. Mutat.*, **31**, 1117–1124.
11. Edener, U., Wollner, J., Hehr, U., Kohl, Z., Schilling, S., Kreuz, F., Bauer, P., Bernard, V., Gillessen-Kaesbach, G. and Zuhlke, C. (2010) Early onset and slow progression of SCA28, a rare dominant ataxia in a large four-generation family with a novel AFG3L2 mutation. *Eur. J. Hum. Genet.*, **18**, 965–968.
12. Pierson, T.M., Adams, D., Bonn, F., Martinelli, P., Cherukuri, P.F., Teer, J.K., Hansen, N.F. and Cruz, P., Mullikin For The Nisc Comparative Sequencing Program, J.C., Blakesley, R.W. *et al.* (2011) Whole-exome sequencing identifies homozygous AFG3L2 mutations in a spastic ataxia-neuropathy syndrome linked to mitochondrial m-AAA proteases. *PLoS Genet.*, **7**, e1002325.
13. Koppen, M., Metodiev, M.D., Casari, G., Rugarli, E.I. and Langer, T. (2007) Variable and tissue-specific subunit composition of mitochondrial m-AAA protease complexes linked to hereditary spastic paraplegia. *Mol. Cell Biol.*, **27**, 758–767.
14. Maltecca, F., Magnoni, R., Cerri, F., Cox, G.A., Quattrini, A. and Casari, G. (2009) Haploinsufficiency of AFG3L2, the gene responsible for spinocerebellar ataxia type 28, causes mitochondria-mediated Purkinje cell dark degeneration. *J. Neurosci.*, **29**, 9244–9254.
15. Custer, S.K., Garden, G.A., Gill, N., Rueb, U., Libby, R.T., Schultz, C., Guyenet, S.J., Deller, T., Westrum, L.E., Sopher, B.L. *et al.* (2006)

Bergmann glia expression of polyglutamine-expanded ataxin-7 produces neurodegeneration by impairing glutamate transport. *Nat. Neurosci.*, **9**, 1302–1311.
16. Mansouri, B., Henne, W.M., Oomman, S.K., Bliss, R., Attridge, J., Finckbone, V., Zeitouni, T., Hoffman, T., Bahr, B.A., Strahlendorf, H.K. *et al.* (2007) Involvement of calpain in AMPA-induced toxicity to rat cerebellar Purkinje neurons. *Eur. J. Pharmacol.*, **557**, 106–114.
17. Duchen, M.R. (2000) Mitochondria and calcium: from cell signalling to cell death. *J. Physiol.*, **529**, 57–68.
18. Berridge, M.J., Bootman, M.D. and Roderick, H.L. (2003) Calcium signalling: dynamics, homeostasis and remodelling. *Nat. Rev. Mol. Cell Biol.*, **4**, 517–529.
19. Ito, M. (2002) The molecular organization of cerebellar long-term depression. *Nat. Rev. Neurosci.*, **3**, 896–902.
20. De Stefani, D., Raffaello, A., Teardo, E., Szabo, I. and Rizzuto, R. (2011) A forty-kilodalton protein of the inner membrane is the mitochondrial calcium uniporter. *Nature*, **476**, 336–340.
21. Perocchi, F., Gohil, V.M., Girgis, H.S., Bao, X.R., McCombs, J.E., Palmer, A.E. and Mootha, V.K. (2010) MICU1 encodes a mitochondrial EF hand protein required for Ca(2+) uptake. *Nature*, **467**, 291–296.
22. Szabadkai, G., Simoni, A.M., Chami, M., Wieckowski, M.R., Youle, R.J. and Rizzuto, R. (2004) Drp-1-dependent division of the mitochondrial network blocks intraorganellar Ca2+ waves and protects against Ca2+-mediated apoptosis. *Mol. Cell*, **16**, 59–68.
23. Chiesa, A., Rapizzi, E., Tosello, V., Pinton, P., de Virgilio, M., Fogarty, K.E. and Rizzuto, R. (2001) Recombinant aequorin and green fluorescent protein as valuable tools in the study of cell signalling. *Biochem. J.*, **355**, 1–12.
24. Glitsch, M.D., Bakowski, D. and Parekh, A.B. (2002) Store-operated Ca2+ entry depends on mitochondrial Ca2+ uptake. *EMBO J.*, **21**, 6744–6754.
25. Nicholls, D.G. (1974) The influence of respiration and ATP hydrolysis on the proton-electrochemical gradient across the inner membrane of rat-liver mitochondria as determined by ion distribution. *Eur. J. Biochem./FEBS*, **50**, 305–315.
26. Irwin, W.A., Bergamin, N., Sabatelli, P., Reggiani, C., Megighian, A., Merlini, L., Braghetta, P., Columbaro, M., Volpin, D., Bressan, G.M. *et al.* (2003) Mitochondrial dysfunction and apoptosis in myopathic mice with collagen VI deficiency. *Nat. Genet.*, **35**, 367–371.
27. Bernardi, P. (1999) Mitochondrial transport of cations: channels, exchangers, and permeability transition. *Physiol. Rev.*, **79**, 1127–1155.
28. Frieden, M., James, D., Castelbou, C., Danckaert, A., Martinou, J.C. and Demaurex, N. (2004) Ca(2+) homeostasis during mitochondrial fragmentation and perinuclear clustering induced by hFis1. *J. Biol. Chem.*, **279**, 22704–22714.
29. Ehses, S., Raschke, I., Mancuso, G., Bernacchia, A., Geimer, S., Tondera, D., Martinou, J.C., Westermann, B., Rugarli, E.I. and Langer, T. (2009) Regulation of OPA1 processing and mitochondrial fusion by m-AAA protease isoenzymes and OMA1. *J. Cell Biol.*, **187**, 1023–1036.
30. Song, Z., Chen, H., Fiket, M., Alexander, C. and Chan, D.C. (2007) OPA1 processing controls mitochondrial fusion and is regulated by mRNA splicing, membrane potential, and Yme1L. *J. Cell Biol.*, **178**, 749–755.
31. Akepati, V.R., Muller, E.C., Otto, A., Strauss, H.M., Portwich, M. and Alexander, C. (2008) Characterization of OPA1 isoforms isolated from mouse tissues. *J. Neurochem*, **106**, 372–383.
32. Duvezin-Caubet, S., Jagasia, R., Wagener, J., Hofmann, S., Trifunovic, A., Hansson, A., Chomyn, A., Bauer, M.F., Attardi, G., Larsson, N.G. *et al.* (2006) Proteolytic processing of OPA1 links mitochondrial dysfunction to alterations in mitochondrial morphology. *J. Biol. Chem.*, **281**, 37972–37979.
33. Rizzuto, R., Pinton, P., Carrington, W., Fay, F.S., Fogarty, K.E., Lifshitz, L.M., Tuft, R.A. and Pozzan, T. (1998) Close contacts with the endoplasmic reticulum as determinants of mitochondrial Ca2+ responses. *Science*, **280**, 1763–1766.
34. Csordas, G., Varnai, P., Golenar, T., Roy, S., Purkins, G., Schneider, T.G., Balla, T. and Hajnoczky, G. (2010) Imaging interorganelle contacts and local calcium dynamics at the ER-mitochondrial interface. *Mol. Cell*, **39**, 121–132.
35. de Brito, O.M. and Scorrano, L. (2008) Mitofusin 2 tethers endoplasmic reticulum to mitochondria. *Nature*, **456**, 605–610.
36. Manders, E.M., Verbeek, F.J. and Aten, A. (1993) Measurement of colocalization of objects in dual color confocal images. *J. Microsc.*, **169**, 375–382.
37. Yamaguchi, R., Lartigue, L., Perkins, G., Scott, R.T., Dixit, A., Kushnareva, Y., Kuwana, T., Ellisman, M.H. and Newmeyer, D.D. (2008) Opa1-mediated cristae opening is Bax/Bak and BH3 dependent, required for apoptosis, and independent of Bak oligomerization. *Mol. Cell*, **31**, 557–569.
38. Cipolat, S., Martins de Brito, O., Dal Zilio, B. and Scorrano, L. (2004) OPA1 requires mitofusin 1 to promote mitochondrial fusion. *Proc. Natl Acad. Sci. USA*, **101**, 15927–15932.
39. Legros, F., Lombes, A., Frachon, P. and Rojo, M. (2002) Mitochondrial fusion in human cells is efficient, requires the inner membrane potential, and is mediated by mitofusins. *Mol. Biol. Cell*, **13**, 4343–4354.
40. Misaka, T., Miyashita, T. and Kubo, Y. (2002) Primary structure of a dynamin-related mouse mitochondrial GTPase and its distribution in brain, subcellular localization, and effect on mitochondrial morphology. *J. Biol. Chem.*, **277**, 15834–15842.
41. Baricault, L., Segui, B., Guegand, L., Olichon, A., Valette, A., Larminat, F. and Lenaers, G. (2007) OPA1 cleavage depends on decreased mitochondrial ATP level and bivalent metals. *Exp. Cell Res.*, **313**, 3800–3808.
42. Griparic, L., Kanazawa, T. and van der Bliek, A.M. (2007) Regulation of the mitochondrial dynamin-like protein Opa1 by proteolytic cleavage. *J. Cell Biol.*, **178**, 757–764.
43. Chen, H., McCaffery, J.M. and Chan, D.C. (2007) Mitochondrial fusion protects against neurodegeneration in the cerebellum. *Cell*, **130**, 548–562.
44. Schuermann, M. (1990) An expression vector system for stable expression of oncogenes. *Nucleic Acids Res.*, **18**, 4945–4946.
45. Schoenmakers, T.J., Visser, G.J., Flik, G. and Theuvenet, A.P. (1992) CHELATOR: an improved method for computing metal ion concentrations in physiological solutions. *Biotechniques*, **12**, 870–874, 876–879.